Toward the *In Situ* Detection of Individual He_2^* Excimers Using a Ti TES in Superfluid Helium

Faustin W. Carter, Scott A. Hertel, Michael J. Rooks, Daniel N. McKinsey, and Daniel E. Prober

(Invited Paper)

***Abstract*—We characterize a single titanium (Ti) transition edge sensor (TES) designed for *in situ* detection of individual He_2^* excimers. We find a critical temperature of 420 mK, an electrothermal time constant of $\sim$3 μs, and a total energy resolution of 1.5 eV. We observe the detector response to short laser pulses and present a successful analysis strategy for extracting direct-TES-hit pulses from a much larger background (due to substrate hits). We also present the response of a similar Ti TES with a built-in aperture designed to eliminate substrate background; this device has an energy resolution of better than 1.5 eV and a much reduced substrate signal. We discuss near-term plans for coupling multiple such TESs together with a shared aluminum (Al) absorber, increasing the He_2^* collection area to millimeter scales.**

***Index Terms*—Helium excimer, transition edge sensor (TES), UV sensor.**

I. Introduction

THE dynamics of quantum turbulence in superfluid ^{4}He is a field of active research. Quantum vortices are made observable by trapping particles within the vortex core. The particles used for tagging the vortices in this way would ideally be easily observed, long-lived, and small in diameter so as not to perturb the vortex dynamics under study. Micron-scale hydrogen ice particles have been used [1], [2], but He_2^* excimers, produced *in situ* through electron bombardment [3]–[5] or laser ionization [6] offer significant advantages. Due to extremely weak spin-orbit coupling, this triplet He_2 $(a^3\Sigma_u^+)$ state is metastable, with a lifetime of 13 s [7]. This state is 17.8 eV above ground, and releases photons spread in energy over a broad UV peak (13–18 eV) upon decay [8]. It releases a similar energy when non-radiatively quenched on a solid surface [9]. He_2^* is efficiently and permanently trapped by quantum vortices (trapping radius $\sim$100 nm [10]). Although there are ongoing efforts to observe this trapped state using laser fluorescence [11], [12], to date this trapped state has been observed only through surface quenching [10], [13].

We aim to improve on the previous surface quenching observation studies through the use of a calorimetric sensing technique (which is sensitive to direct photon absorption as well as surface quenching). While the current-sensing apparatus of Zmeev *et al.* [10], [13] is the state of the art and has produced significant new results, the charge-sensing technique suffers from low efficiency $(\leq 10^{-3})$ [14], and the resulting signals are, by necessity, averaged over many instances of quantum turbulence production spanning several days. Here, we describe progress toward measuring a He_2^* flux using a TES sensor coupled to a large-area Al absorber, a technique which promises near unity intrinsic efficiency and should be capable of observing quantum turbulence dynamics on much shorter time scales.

The goal of this paper is to describe a preliminary characterization of the bare TES (TES A) in the absence of any Al absorbing fins. We present the detector noise and signal response to a pulsed blue laser (470 nm) in vacuum, as well as a method for using the RMS fluctuations to distinguish the TES photon signal from a large unwanted background signal in the absence of a calibrated single-photon source. We justify this approach by presenting data from a similar TES (TES B) that has been engineered to avoid the unwanted substrate signal.

II. TES Detectors

A. Design

A well-designed TES is dominated by intrinsic thermal fluctuation noise, which is a strong function of the TES operating temperature T_c [15]. Some of the more common materials for TES fabrication are molybdenum/gold (Mo/Au) [16], titanium/gold (Ti/Au), and tungsten (W) [17]. We have decided for this demonstration project to employ a material that is well characterized in our laboratory, elemental titanium (Ti) [18], [19]. Although Ti has a critical temperature $(T_c \approx 350\,\text{mK})$ that is somewhat higher than other options, its T_c is reproducible, avoiding the complexities of the variable (or, tunable) T_c values of Mo/Au, W, or Ti/Au. Our Ti TESs should still be sensitive to the 15 eV energy we expect from an excimer decay.

Thermal fluctuation noise in hot-electron-style TESs is also a function of electron heat capacity, and therefore detector volume; TESs are typically made as small as possible (subject to retaining a linear response) in order to limit this noise [15]. To obtain a large signal collection area despite the sensor's small size, it is advantageous to employ an absorber that collects the photon or excimer energy and couples this energy

Manuscript received August 13, 2014; accepted November 11, 2014. Date of publication November 20, 2014; date of current version December 15, 2014. This work was supported in part by YINQE and NSF MRSEC DMR-1119826 and in part by the National Science Foundation under NSF DMR-1007974.

The authors are with Yale University, New Haven, CT 06520-8284 USA (e-mail: faustin.carter@yale.edu).

Color versions of one or more of the figures in this paper are available online at http://ieeexplore.ieee.org.

Digital Object Identifier 10.1109/TASC.2014.2372673

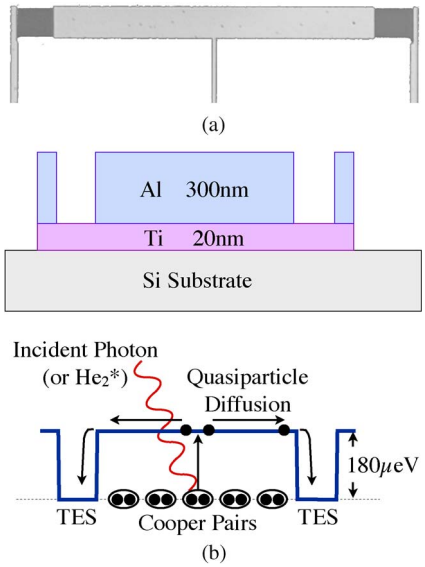

Fig. 1. (a) Optical microscope image (false color) showing an actual device. The Ti TESs are the gray squares and are 20×20 μm^2. (b) (Top) Schematic of the detector cross section. (Bottom) Energy-level diagram showing the energy gap of the Al and the lower energy trapping regions of the Ti TESs, with nearly zero gap at their T_c.

into the TES. We are following a general approach currently in use by CDMS [20], and previously at Yale [21]–[23] wherein a superconducting absorber is coupled to the TES; the absorber is aluminum (Al) in our case. The absorbed energy breaks Cooper pairs in the Al, and the resulting quasiparticles diffuse within the Al and are eventually trapped by the TES [24]. This process is depicted in Fig. 1. In previous work we have measured the quasiparticle lifetime of our evaporated Al films to be quite long, allowing for a large ($\sim$1 mm) absorber [25], [26]. If a single Al absorber is connected to multiple TESs, the position of the energy deposition in the absorber can be determined by comparing the relative pulse energies [20], [22], [27].

B. Fabrication

The present detectors are fabricated by evaporating a titanium/aluminum (Ti/Al) bilayer onto a high-resistivity silicon (Si) wafer through a poly-methyl-methacrylate (PMMA) lift-off mask defined by electron-beam lithography. The process has three steps; two lift-off steps, and one etch step. The final product is depicted in Figs. 1(a) and 3 (inset); the fabrication process is the same whether or not the absorber fins are included.

1) The Si wafer is first spun with PMMA and a pattern of alignment marks are written with the electron-beam lithography tool (a Raith EBPG). The alignment marks consist of 400 nm of copper (Cu) with a few nanometers of Ti underneath that serves as an adhesion layer. The unwanted metal is then lifted off by dissolving the PMMA mask in N-Methyl-2-pyrrolidone (NMP) that has been heated to 70 °C.
2) The wafer is again spun with PMMA and the detector-cum-absorber pattern is written via EBPG. A bilayer of 20 nm of Ti and 300 nm of Al is evaporated and then lifted off.

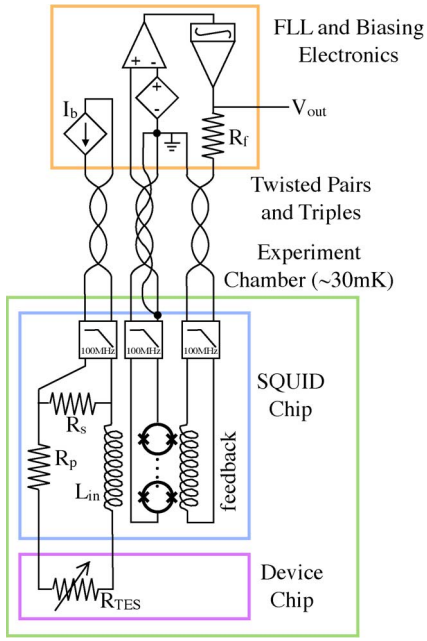

Fig. 2. Electrical readout scheme. The voltage across the feedback resistor is low-pass filtered at 1.9 MHz and read out by a digitizing oscilloscope.

3) Another layer of PMMA is spun, and a window over the Ti TES region is opened via another EBPG write. The exposed Al is removed through a two-minute etch with tetramethyl ammonium hydroxide photoresist developer [28]; this completes the base detector.

Finally, the Si wafer is diced and the device is mounted to the experiment with a dab of GE Varnish [29] and wire-bonded to the board containing the SQUID Amplifiers.

C. Readout

We operate our TESs in the negative electrothermal feedback mode [30] and read them out with a commercial three-channel system. Each channel is read out using a single-stage SQUID amplifier and room-temperature flux locked loop (FLL) electronics [31], [32]. In this configuration the TES is in parallel with a small shunt resistor R_s and in series with an inductor $L = 5$ nH. The TES is voltage biased ($R_{TES} > R_s$). The inductor converts the current through the TES to a magnetic flux, which is then read out by the SQUID. Our output signal is the voltage across the feedback resistor R_f in the flux-locked loop. The circuit diagram is depicted in Fig. 2.

In any real implementation of this circuit, there is some parasitic lead resistance R_p between the TES and the inductor that couples to the SQUID. We have endeavored to use superconducting circuit board traces (tin-coated copper) where possible to minimize this resistance. In our configuration, $R_p = 5$ mΩ.

D. TES Characterization

Here we present the characterization of a single Ti TES (TES A) with Al leads, but no Al absorber fin, as a first step toward understanding the detector behavior. The Ti TES is 40×40 μm^2 and is 20 nm thick. The device is pictured in the

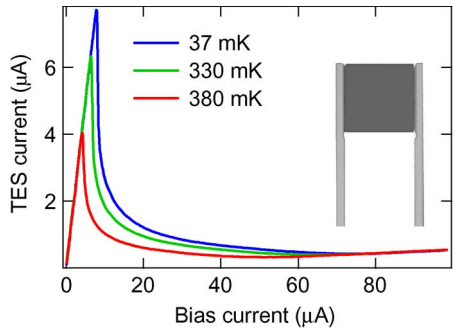

Fig. 3. Current through TES A ($I_{\rm TES}$) as a function of bias current ($I_{\rm b}$). (Inset) Optical microscope image of device. The dark area is the 20-nm-thick Ti TES, which is 40×40 μm^2, and the lighter lengths are 300-nm-thick Al leads.

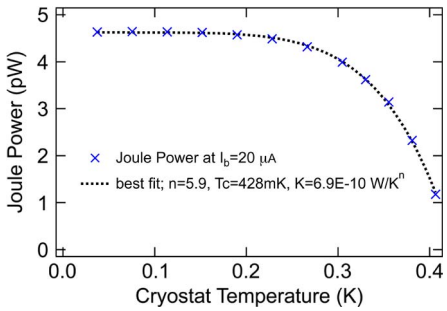

Fig. 4. Joule power dissipated by TES A at constant bias current $I_{\rm b} = 20$ μA at different bath temperatures, fit using (2).

inset of Fig. 3. The Al leads are 300 nm thick, 5 μm wide and serve to contain the hot electrons within the TES so that the primary cooling channel is electron–phonon interaction within the TES rather than electron out-diffusion through the leads. The important quantities for predicting device performance are the heat capacity C, the thermal conductance G, the power-law exponent describing thermal conductance n (see (2)) the constant current logarithmic temperature sensitivity $\alpha_{\rm I}$, and the constant temperature logarithmic current sensitivity $\beta_{\rm I}$. Both $\alpha_{\rm I}$ and $\beta_{\rm I}$ are calculated using partial derivatives, and are related to the total alpha $\alpha_{\rm T}$ (the logarithmic sensitivity as a function of both current and temperature) through

$$\alpha_{\rm T} = \frac{2\alpha_{\rm I} + \frac{n}{\phi}\beta_{\rm I}}{2\beta_{\rm I}} \tag{1}$$

where $\phi = (1 - T_{\rm b}^n/T_{\rm c}^n)$ is a function of both $T_{\rm c}$ and the bath temperature $T_{\rm b}$. $\alpha_{\rm T}$ can be calculated from the curves in Figs. 3 and 4 [33].

Fig. 3 shows the current through the detector $I_{\rm TES}$ as a function of bias current $I_{\rm b}$ at different bath temperatures $T_{\rm b}$. The linear region at $I_{\rm b}$ is when the TES is fully superconducting, and the peak is when $I_{\rm b} = I_{\rm c}$ where $I_{\rm c}$ is the critical current of the TES. A fit to this line gives a measurement of $R_{\rm p}$ provided $R_{\rm s}$ is known. The linear region at high $I_{\rm b}$ is when the TES is fully normal and a fit to this line gives the parallel combination of $R_{\rm s}$ and the TES normal resistance R_n. The smooth downward sloping curve in between the linear regions indicates bias currents for which the TES is biased within its superconducting transition.

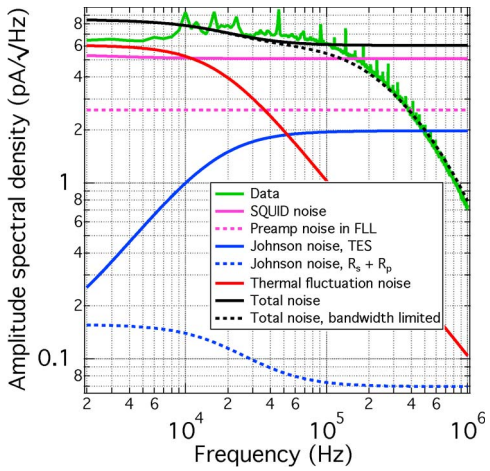

Fig. 5. Detector noise contributions referred to the TES current (TES A).

Because it is not possible to measure $\alpha_{\rm I}$ directly when the TES is configured for electro-thermal feedback, it has been our practice to calculate $\alpha_{\rm T}$ from the $I_{\rm TES}$ vs. $I_{\rm b}$ curve, relate $\beta_{\rm I}$ to $\alpha_{\rm I}$ through (1) and then fit the remaining parameter $\alpha_{\rm I}$ to the measured time constant τ of the TES. The model we use to do these fits is described in Irwin and Hilton [15].

We can calculate the resistance and Joule heating power $P_{\rm J}$ as a functions of $I_{\rm b}$. The optimal bias point for detection is when the power dissipation is flat as a function of $I_{\rm b}$. We have chosen to operate our device at $I_{\rm b} = 20$ μA, which gives us a device resistance $R_{\rm TES} = 3.9$ Ω.

The Joule power input to the TES is $P_{\rm J} = I_{\rm TES}^2 R_{\rm TES}$. In the flat region of the power curve, the TES is biased on its transition at its critical temperature $T_{\rm c}$ and is dissipating 100% of the Joule power via electron–phonon coupling. A power-law dependence for the electron–phonon mediated power loss is assumed and so

$$P_{\rm J} = I_{\rm TES}^2 R_{\rm TES} = K(T_{\rm c}^n - T_{\rm b}^n) \tag{2}$$

where K is the electron–phonon coupling constant for the TES and n is an exponent that depends on the mechanism of power loss [15]. Most TESs have an n between 3–6. In order to determine the thermal conductivity of our TES at its bias point of 20 μA, we measure $P_{\rm J}$ vs. $T_{\rm b}$ and fit it to (2) to determine K and n. The thermal conductivity at the operating point is then given by $G = dP_{\rm J}/dT_{\rm b}|_{T_{\rm b}=T_{\rm c}} = nKT_{\rm c}^{n-1}$. The data and the fit are shown in Fig. 4.

We have used these measured parameters to estimate the device noise, and compare it to actual noise measurements. Fig. 5 depicts the various expected contributions to the overall noise referred to the current through the TES as well as the actual measured current noise. The equations for the various noise contributions are found in Irwin and Hilton [15].

E. Device Response to Blue Laser Pulses

Here we present the response of two different single pixel TESs to blue laser light. The first, TES A, is the one described in the previous section (see Fig. 3). The second, TES B, is nearly identical, but smaller; it is only 20×20 μm^2. TES B also has

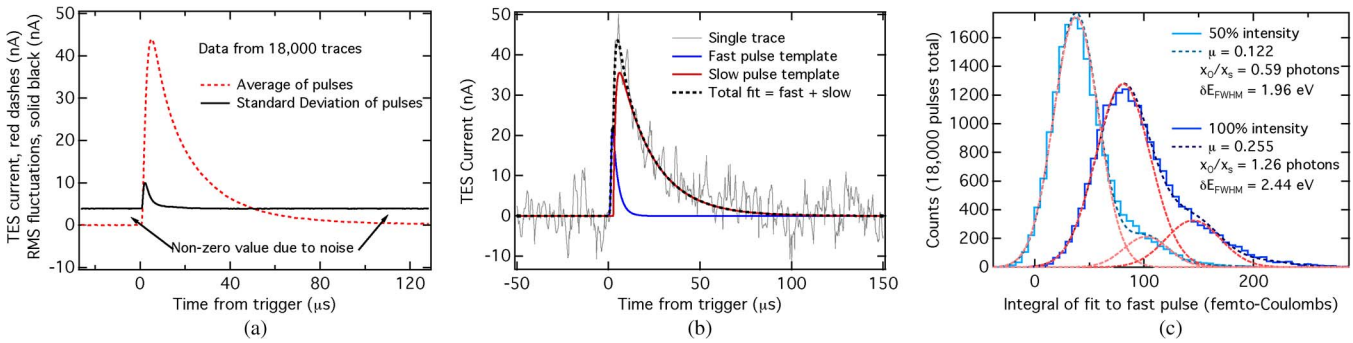

Fig. 6. (a) Average and standard deviation of 18 000 pulses at full intensity for TES A. (b) Example of the model used to fit the pulse data from TES A. (c) Histograms of integrals of the fast pulse fits for TES A. These histograms are fit by (3); one photon corresponds to 64.1 fC. The dashed red curves show the first two terms $(n = 0, n = 1)$ of each fit.

a built-in aperture that shields the substrate from photon hits and only allows light through to the TES. Data from a two-TES device with an Al absorber will be presented in a future publication.

The data presented in this section were taken by passing short pulses from a blue laser (470 nm, 2.64 eV) through a bank of adjustable neutral density filters, which couple into an optical fiber that terminates ∼2 cm above the TES. We triggered the oscilloscope on the laser pulse. We took pulse data at multiple attenuations. We refer to the brightest setting as full intensity and dimmer settings are labeled as a percentage of the full intensity setting.

1) TES A: For TES A, the bare $40 \times 40\ \mu\text{m}^2$ TES, 18 000 pulses were recorded for two attenuation settings (full and 50%). Fig. 6(a) shows the average of 18 000 pulses and the standard deviation of pulses for the full intensity case. The corresponding curves calculated from the 50% attenuated pulses are characteristically similar in shape to those in Fig. 6(a), but roughly half as large in amplitude (the pre- and post-pulse flat sections of the standard deviation, which describes the system noise, are the same for both attenuations).

At long time scales $(> 10\ \mu\text{s})$, the pulses are well described by a falling exponential and are precisely repeatable, as can be seen in the standard deviation during this time, which is consistent with the pre-pulse noise. At short times $(< 10\ \mu\text{s})$, the standard deviation reveals interesting variation between laser pulses, with a falling time constant suggestive of the TES intrinsic fall time of a few microseconds (calculated from C, G, and α_T). Our interpretation is that the large, slow pulse is the result of energy delivered to the TES in the form of phonons, resulting from the large incident photon flux on the substrate. The faster, smaller component (the component which varies from pulse to pulse) is interpreted as arising from direct photon hits to the TES. The small, fast pulses are the more interesting component of the data, as they should obey Poisson statistics and can also be directly modeled by the equations in Irwin and Hilton [15].

We claim that the standard deviation can be used as a model pulse template for the fast component. In order to show this, we assume three sources of fluctuations in our pulses: fluctuations due to noise that is not related to the photon pulses σ_{N}, fluctuations due to a varying amount of power absorbed by the substrate σ_{Si}, and fluctuations due to the varying number of photons directly absorbed in the detector σ_{TES}. If we assume these three sources of fluctuations are uncorrelated then they add in quadrature and the total RMS fluctuations (plotted in Fig. 6, black curve) are described by $\sigma^2 = \sigma_{\text{N}}^2 + \sigma_{\text{Si}}^2 + \sigma_{\text{TES}}^2$; this equation is easily rearranged to give σ_{TES} as a function of the other variables. Since the standard deviation of a set of exponential pulses with different amplitudes, but identical rise and fall times, is an exponential pulse of the same character, σ_{TES} is therefore an excellent template for the fast pulse that contains the information about direct photon hits to the TES. From Fig. 6 it is clear that $\sigma_{\text{Si}} < \sigma_{\text{N}}$ (since there is no apparent variation on the 20 μs timescale) and that σ_{N} is constant over time, and so the model for our pulse template (σ_{TES}) is easily computed.

We used a double exponential pulse shape to fit the rise and fall of σ_{TES} and used this fit function as a template to extract the fast pulse component from each individual trace. We fixed the decay time, rise time, and starting time of the template, while allowing the amplitude to vary. Once we had a model for the fast pulse, we were able to use that along with the average of the data to infer a model for the slow pulse (also a double exponential). Finally, the slow pulse template parameters were fixed, save for the amplitude, and the model (now with only the two model pulse amplitudes as free parameters) was fit to all 18 000 traces. One of these fits is depicted in Fig. 6(b). The fast pulse fits were then integrated and histograms were made for both attenuations [Fig. 6(c)].

The histograms were fit to the first 20 terms of a Gaussian-broadened Poisson distribution

$$f(x) = \frac{A}{\sigma_{\text{s}}\sqrt{2\pi}} \sum_{n=1}^{20} \frac{e^{-\mu}\mu^n}{n} \exp\left(-\frac{(x - x_0 - nx_{\text{s}})^2}{2(\sigma_{\text{s}})^2}\right) \quad (3)$$

where μ is average photon number, x_{s} is a scale factor that relates pulse integral to photon number, x_0 is an offset, and $\sigma_{\text{s}} = x_{\text{s}} * \delta E_{\text{FWHM}}/(E_0 * 2\sqrt{2\ln 2})$ is related to the full-width at half-maximum (FWHM) energy resolution δE_{FWHM} of the detector as well as the deposited photon energy E_0. The initial guess for x_{s} was calculated by plugging all the measured device parameters into the Irwin and Hilton models, generating a

TABLE I
TES RESPONSE TO BLUE PHOTONS. μ IS AVERAGE PHOTON NUMBER, x_0 IS THE OFFSET OF THE HISTOGRAM FROM ZERO

Device	μ (photons)	x_0/μ	δE_{FWHM}
TES A (no shield)	0.12	4.9	1.96 eV
	0.26	4.9	2.44 eV
TES B (shield)	0.12	0.6	1.23 eV
	0.25	0.6	1.33 eV
	0.40	0.6	1.49 eV

model pulse for a single photon, and integrating the model. Likewise, the initial guess for σ_{s} was calculated from the Irwin and Hilton model. The scale factor A is a fixed parameter and is equal to the area of the histogram being fit. We summarize the relevant fit results in Table I.

We can calculate δE_{FWHM} from σ_{s}. For the full intensity histogram, $\sigma = \sigma_{\mathrm{s}}/x_{\mathrm{s}} = 0.39$ and $\delta E_{\mathrm{FWHM}} = 2.44$ eV. We can compare this to the intrinsic device resolution calculated from the Irwin and Hilton model, $\delta E_{\mathrm{FWHM}} = 0.6$ eV. The full system resolution is roughly four times worse than the theoretical value from the Irwin and Hilton model, but that is reasonable given that over much of our bandwidth we are dominated by amplifier and electronic noise (see Fig. 5) rather than intrinsic TES noise.

The fact that x_0 and a component of δE_{FWHM} (Table I) are both linearly proportional to μ implies that there is some extra signal that is unaccounted for in our two-pulse model. If we imperfectly subtract the constant external input from substrate events, then there will be a residual amount of energy in every pulse. This residual energy will be constant across measured pulses, independent of how many photons directly hit the TES, and will manifest as a constant offset from zero for the histogram that scales with laser intensity. We can estimate TES A's energy resolution in the absence of a substrate signal by fitting a straight line to a plot of δE_{FWHM} vs. μ, and extracting the y-intercept. This calculation gives $\delta E_{\mathrm{FWHM}} = 1.52$ eV.

2) TES B: To observe the behavior of a TES in the absence of substrate hits, we constructed a new detector (TES B) with a shield by depositing a Cu/Al bilayer (50 nm of each) over a one micron thick layer of PMMA and etching a square aperture directly over the TES. TES B is identical to TES A except it is 20×20 μm^2. The laser pulse experiment was repeated with TES B, and 10 000 pulses each at three different laser intensities were collected. Fig. 7 shows histograms of pulse integrals for the different intensities. For this TES, the data analysis is much simpler. In the absence of a large substrate signal, we were able to simply integrate each raw pulse and then construct a histogram of the integrals.

Despite the shield, there is still a small offset that scales with intensity. However, it is smaller by nearly an order of magnitude than the residual offset from our best fits for TES A. In fact, if we account for the size difference between TESs A and B and normalize the offset by TES volume, the shield reduces the offset by a factor of about 30. When we average the pulses in the FWHM of the zero-photon peak, we find that the zero-photon pulse average has a slower rise time and much slower fall time than the pulses in the other peaks. This is because it is entirely due to substrate heating, rather than a direct TES hit. The substrate heating arises because we did not heat-sink the shield very well; it must eventually cool by emitting phonons through the PMMA and into the substrate.

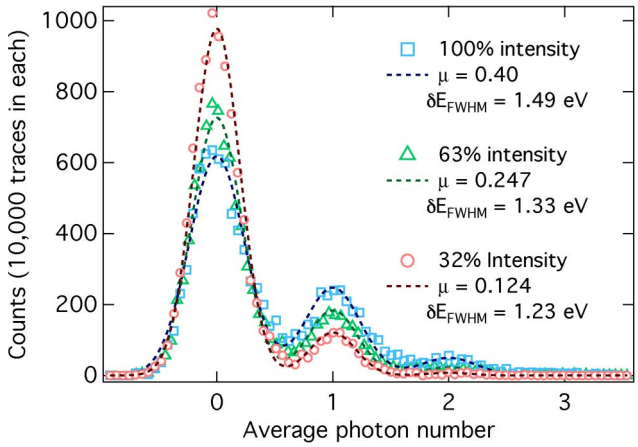

Fig. 7. Histograms of raw pulse integrals for shielded 20×20 μm^2 TES (TES B). Each histogram x-axis was shifted by the zero-photon peak offset, normalized by the one-photon peak value, and fit to (3).

The histograms in Fig. 7 were constructed by subtracting the zero-photon peak value from each raw histogram, and then normalizing by the average value contained within the FWHM of the one-photon peak. After normalizing, each histogram was fit by (3); the only free parameters were μ and σ_{s} (subtracting the offset before fitting means $x_0 = 0$ for the fit). These fits overlay the data in Fig. 7, and the fit parameters are listed in Table I; σ_{s} has been converted to δE_{FWHM} for clarity, and the x_0 parameter listed for TES B corresponds to the original position of the zero-photon peak.

III. CONCLUSION

1) The two-pulse model works well for extracting TES hits from underneath substrate hits, and is a useful method for characterizing unshielded devices like TES A. Pulse data from TES B justifies this approach. The average pulse energy for pulses in the one-photon peaks of TES B (Fig. 7) is consistent with the pulse energy contained in our one-photon model pulse for TES A (Fig. 6)—roughly 1.5 eV in both cases. The fact that only about 0.6 of the photon energy couples to the detector is expected due to phonon emission during electron energy sharing [34].
2) A smaller TES with a shield that eliminates photon absorption in the substrate is much better. In Fig. 5 the thermal fluctuation noise is slightly above the electronic noise at low frequencies. Making the TES smaller brings this contribution down and then the signal is truly amplifier-limited. Adding a shield removes most (90%) of the large slow pulse. This improves the resolution to better than 1.5 eV FWHM (Fig. 7, Table I).
3) A Ti TES should indeed be capable of resolving individual $He_2{}^*$ excimers ($\sim$15 eV). Despite the relatively high critical temperature of Ti, our analysis shows that this simple elemental TES will provide sufficient resolution

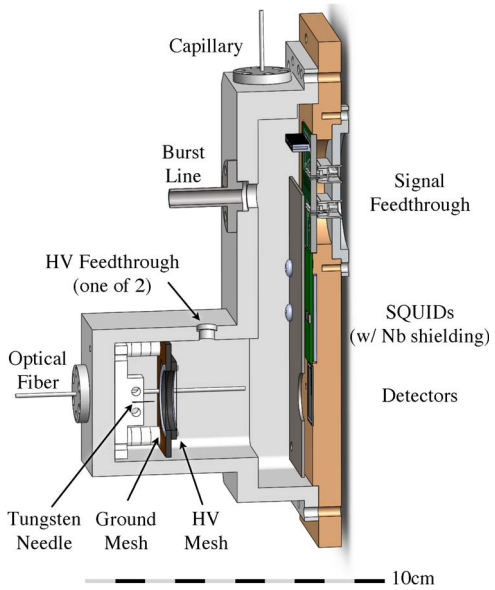

Fig. 8. Rendering of the experimental chamber. HV is high voltage (∼kV). The baseplate is oxygen-free high thermal conductivity (OFHC) copper, the L-shaped top cap is machined from a block of aluminum, and the two are bolted together with an indium seal. The assembly is mounted in the depicted orientation on the cold plate of a dilution refrigerator.

to discriminate individual He_2 excimers (or any other quantized UV signal). This will also be true for the Al absorber coupled TESs we plan to study next.

Appendix
Experimental Chamber Design

The experiment design posed several technical challenges, many the result of staging a complex process in a superfluid bath that can leak through even the smallest gaps. A full description of the system will be provided in a future publication. Fig. 8 shows a computer rendering of the experimental chamber. Here we describe briefly the fiber optic system.

We use a multi-mode fiber with a 300 μm diameter [35]. The fiber enters the cryostat through a hermetic seal at room temperature [36]. We have found that heat-sinking the fiber is unnecessary. The fiber enters the experimental chamber through a superfluid-tight feedthrough, created following the procedure of J.S. Butterworth *et al.* [37], in which the seal is made through the thermal contraction of a length of heat-shrink tubing [38] during cool down. The fiber is intended only as a tool for device characterization; it should not interfere with the TESs ability to collect $He_2{}^*$ excimers or EUV photons released on excimer decay. For this reason we have suspended the cleaved end of the fiber a few centimeters from the TES to keep it out of the way.

Acknowledgment

The authors would like to thank J. Cushman for drafting expertise; C. Matulis for circuit-board design; Dr. L. Frunzio for fabrication advice; Prof. R. Schoelkopf, Prof. M. Devoret, and Prof. M. Hatridge for cryogenics expertise; C. McKitterick, Dr. Z. Leghtas, and S. Touzard for helpful discussions; and the Gibbs Machine Shop for many parts.

References

[1] G. P. Bewley, D. P. Lathrop, and K. R. Sreenivasan. (2006, Jun.). Superfluid helium: Visualization of quantized vortices. *Nature* [Online]. *441(7093)*, p. 588. Available: http://www.ncbi.nlm.nih.gov/pubmed/16738652

[2] Y. A. Sergeev and C. F. Barenghi. (2009, Dec.). Particles–vortex interactions and flow visualization in ^{4}He. *J. Low Temperature Phys.* [Online]. *157(5/6)*, pp. 429–475. Available: http://link.springer.com/10.1007/s10909-009-9994-8

[3] J. Keto, M. Stockton, and W. Fitzsimmons. (1972, Mar.). Dynamics of atomic and molecular metastable states produced in electron-bombarded superfluid helium. *Phys. Rev. Lett.* [Online]. *28(13)*, pp. 792–795. Available: http://link.aps.org/doi/10.1103/PhysRevLett.28.792

[4] J. Keto, F. Soley, M. Stockton, and W. Fitzsimmons. (1974, Sep.). Dynamic properties of neutral excitations produced in electron-bombarded superfluid helium. I. The He($2\,^3$S) and He_2 ($a^3\Sigma$) atomic and molecular metastable states. *Phys. Rev. A* [Online]. *10(3)*, pp. 872–886. Available: http://link.aps.org/doi/10.1103/PhysRevA.10.872

[5] D. Tokaryk, R. Brooks, and J. Hunt. (1993, Jul.). Reaction dynamics of metastable helium molecules and atoms near 4.2 K. *Phys. Rev. A* [Online]. *48(1)*, pp. 364–381. Available: http://link.aps.org/doi/10.1103/PhysRevA.48.364

[6] A. V. Benderskii, R. Zadoyan, N. Schwentner, and V. A. Apkarian. (1999, Jan.). Photodynamics in superfluid helium: Femtosecond laser-induced ionization, charge recombination, and preparation of molecular Rydberg states. *J. Chemical Phys.* [Online]. *110(3)*, pp. 1542–1557. Available: http://scitation.aip.org/content/aip/journal/jcp/110/3/10.1063/1.477796

[7] D. McKinsey *et al.* (1999, Jan.). Radiative decay of the metastable He_2 ($a^3\Sigma_u^+$) molecule in liquid helium. *Phys. Rev. A* [Online]. *59(1)*, pp. 200–204. Available: http://link.aps.org/doi/10.1103/PhysRevA.59.200

[8] M. Stockton, J. Keto, and W. Fitzsimmons. (1970, Mar.). Ultraviolet emission spectrum of electron-bombarded superfluid helium. *Phys. Rev. Lett.* [Online]. *24(12)*, pp. 654–657. Available: http://link.aps.org/doi/10.1103/PhysRevLett.24.654

[9] M. I. Trioni, G. Butti, N. Bonini, and G. P. Brivio. (2005, Aug.). Metastable helium spectroscopy on simple metals: Comparison between low and high work function substrates. *Surface Sci.* [Online]. *587(1/2)*, pp. 121–127. Available: http://linkinghub.elsevier.com/retrieve/pii/S0039602805004474

[10] D. E. Zmeev *et al.* (2013, Apr.). Excimers $He_2{}^*$ as tracers of quantum turbulence in ^{4}He in the $T = 0$ limit. *Phys. Rev. Lett.* [Online]. *110(17)*, Art. ID. 175303. Available: http://link.aps.org/doi/10.1103/PhysRevLett.110.175303

[11] W. Rellergert *et al.* (2008, Jan.). Detection and imaging of He_2 molecules in superfluid helium. *Phys. Rev. Lett.* [Online]. *100(2)*, Art. ID. 025301. Available: http://link.aps.org/doi/10.1103/PhysRevLett.100.025301

[12] D. McKinsey, W. Lippincott, J. Nikkel, and W. Rellergert. (2005, Sep.). Trace detection of metastable helium molecules in superfluid helium by laser-induced fluorescence. *Phys. Rev. Lett.* [Online]. *95(11)*, Art. ID. 111101. Available: http://link.aps.org/doi/10.1103/PhysRevLett.95.111101

[13] D. E. Zmeev *et al.* (2012, May). Observation of crossover from ballistic to diffusion regime for excimer molecules in superfluid ^{4}He. *J. Low Temperature Phys.* [Online]. *171(3/4)*, pp. 207–213. Available: http://link.springer.com/10.1007/s10909-012-0720-6

[14] R. Mehrotra, E. K. Mann, and A. J. Dahm. (1979, Aug.). A study of the neutral excitation current in liquid ^{4}He above 1 K. *J. Low Temperature. Phys.* [Online]. *36(1/2)*, pp. 47–65. Available: http://http://link.springer.com/article/10.1007/%2FBF00174911

[15] K. Irwin and G. Hilton, "Transition-edge sensors," in *Cryogenic Particle Detection*, C. Enss, Ed. Berlin, Germany: Springer-Verlag, 2005, pp. 63–150. [Online]. Available: http://link.springer.com/chapter/10.1007/10933596_3

[16] T. C. Chen, F. M. Finkbeiner, A. Bier, and B. DiCamillo. (1999, Nov.). Molybdenum-gold proximity bilayers as transition edge sensors for microcalorimeters and bolometers. *Supercond. Sci. Technol.* [Online]. *12(11)*, pp. 840–842. Available: http://iopscience.iop.org/0953-2048/12/11/344

[17] A. E. Lita *et al.* (2005, Jun.). Tuning of tungsten thin film superconducting transition temperature for fabrication of photon number resolving detectors. *IEEE Trans. Appl. Supercond.* [Online]. *15(2)*, pp. 3528–3531. Available: http://ieeexplore.ieee.org/lpdocs/epic03/wrapper.htm?arnumber=1440433

[18] D. F. Santavicca *et al.*, "Characterization of terahertz single-photon-sensitive bolometric detectors using a pulsed microwave technique," in *Proc. AIP Conf.*, 2009, pp. 72–75.

[19] D. F. Santavicca *et al.* (2010, Feb.). Energy resolution of terahertz single-photon-sensitive bolometric detectors. *Appl. Phys. Lett.* [Online]. *96(8)*, Art. ID. 083505. Available: http://scitation.aip.org/content/aip/journal/apl/96/8/10.1063/1.3336008

[20] M. Pyle *et al.* (2006, Apr.). Quasiparticle propagation in aluminum fins and tungsten TES dynamics in the CDMS ZIP detector. *Nucl. Instrum. Methods Phys. Res. A* [Online]. *559(2)*, pp. 405–407. Available: http://linkinghub.elsevier.com/retrieve/pii/S0168900205024137

[21] L. Li, L. Frunzio, C. Wilson, and D. Prober. (2003, Jun.). Physical properties of the superconducting Ta film absorber of an X-ray photon detector. *IEEE Trans. Appl. Supercond.* [Online]. *13(2)*, pp. 1124–1127. Available: http://ieeexplore.ieee.org/lpdocs/epic03/wrapper.htm?arnumber=1211804

[22] L. Li, L. Frunzio, C. M. Wilson, and D. E. Prober. (2003, Jan.). Quasiparticle nonequilibrium dynamics in a superconducting Ta film. *J. Appl. Phys.* [Online]. *93(2)*, pp. 1137–1141. Available: http://scitation.aip.org/content/aip/journal/jap/93/2/10.1063/1.1533106

[23] L. Li, "X-ray single photon imaging detectors using superconducting tunnel junctions," Ph.D. dissertation, Yale Univ., New Haven, CT, USA, 2003.

[24] K. D. Irwin, S. W. Nam, B. Cabrera, B. Chugg, and B. A. Young. (1995, Nov.). A quasiparticle-trap-assisted transition-edge sensor for phonon-mediated particle detection. *Rev. Sci. Instrum.* [Online]. *66(11)*, pp. 5322–5326. Available: http://scitation.aip.org/content/aip/journal/rsi/66/11/10.1063/1.1146105

[25] C. Wilson, L. Frunzio, and D. Prober. (2001, Aug.). Time-resolved measurements of thermodynamic fluctuations of the particle number in a nondegenerate Fermi gas. *Phys. Rev. Lett.* [Online]. *87(6)*, Art. ID. 067004. Available: http://link.aps.org/doi/10.1103/PhysRevLett.87.067004

[26] C. Wilson and D. Prober. (2004, Mar.). Quasiparticle number fluctuations in superconductors. *Phys. Rev. B* [Online]. *69(9)*, Art. ID. 094524. Available: http://link.aps.org/doi/10.1103/PhysRevB.69.094524

[27] E. Figueroa-Feliciano, "Position-sensitive quantum calorimeters," Ph.D. dissertation, Stanford Univ., Stanford, CA, USA, 2001.

[28] Dow Chemical, part number Microposit MF-312 Developer. [Online]. Available: http://dow.com

[29] LakeShore Cryotronics, part number VGE-7031. [Online]. Available: http://www.lakeshore.com/

[30] K. D. Irwin. (1995, Apr.). An application of electrothermal feedback for high resolution cryogenic particle detection. *Appl. Phys. Lett.* [Online]. *66(15)*, pp. 1998–2000. Available: http://scitation.aip.org/content/aip/journal/apl/66/15/10.1063/1.113674

[31] Magnicon, XXF-1 SQUID Readout Electronics. [Online]. Available: http://www.magnicon.com

[32] D. Drung *et al.* (2007, Jun.). Highly sensitive and easy-to-use SQUID sensors. *IEEE Trans. Appl. Supercond.* [Online]. *17(2)*, pp. 699–704. Available: http://ieeexplore.ieee.org/lpdocs/epic03/wrapper.htm?arnumber=4277368

[33] K. Kinnunen, "Studies of transition-edge sensor physics: Thermal models and noise," Ph.D. dissertation, Univ. Jyväskylä, Jyväskylä, Finland, 2011.

[34] P. Brink, "Non-equilibrium superconductivity induced by X-ray photons," Ph.D. dissertation, Oxford Univ., Oxford, U.K., 1995.

[35] ThorLabs, part number FT300UMT. [Online]. Available: http://www.thorlabs.com/

[36] Ocean Optics, part number VFT-400-UV-16. [Online]. Available: http://www.oceanoptics.com/

[37] J. S. Butterworth *et al.* (1998, Oct.). A demountable cryogenic feedthrough for plastic optical fibers. *Rev. Sci. Instrum.* [Online]. *69(10)*, pp. 3697–3698. Available: http://scitation.aip.org/content/aip/journal/rsi/69/10/10.1063/1.1149161

[38] TE Connectivity, part number MFT-MT1000-NO.2-X-SP. We tried several brands and types of heat shrink tubing. The part listed above is the only one that tested superfluid-leak-tight. [Online]. Available: http://www.te.com/